Centimeter-Scale Suspended Photonic Crystal Mirrors

João P. Moura,[1,*] Richard A. Norte,[1,†,*] Jingkun Guo,[1] Clemens Schäfermeier,[1] and Simon Gröblacher[1,‡]

[1] *Kavli Institute of Nanoscience, Delft University of Technology, Lorentzweg 1, 2628CJ Delft, The Netherlands*

Demand for lightweight, highly reflective and mechanically compliant mirrors for optics experiments has recently seen a significant surge. Due to their bulky geometry, standard mirror solutions have a high mass, which severely limits their use in applications such as light sails [1], evanescent field sensors [2, 3], or deformable mirrors [4]. Advances in nanofabrication have shown that photonic crystal (PhC) membranes [5] are an ideal alternative to conventional mirrors, as they provide high reflectivity with only a single layer of dielectric material. In particular, devices made of silicon nitride constitute the state-of-the-art in PhC mirrors with low optical absorption and mechanical loss [6–8]. However, fabrication technology has constrained their effective area to a few square-micrometers. Here we experimentally demonstrate the first example of suspended PhC mirrors spanning areas up to $10 \times 10\,\mathrm{mm}^2$. We overcome the limitations imposed by the finite size of the PhC, which allows us to measure reflectivities greater than 99 % on 210 nm thin devices at 1550 nm wavelength and beyond 90 % on 56 nm thick mirrors – an unrivaled performance compared to PhC mirrors with micro scale diameters. We also consider their use as mirrors in gravitational wave detectors where they could potentially reduce mirror coating noise at cryogenic temperatures. These structures bridge the gap between nano scale technologies and macroscopic optical elements.

Photonic crystal (PhC) membranes are suspended dielectric sheets patterned with sub-wavelength, low-index two-dimensional periodic structures [5]. These patterns give rise to resonances that can couple out-of-plane radiation to in-plane guided modes, and can be engineered to transform a flat membrane into a mirror [9], a lens [10], or even a curved mirror [10–12]. Here we study a PhC consisting of a periodic lattice of holes in a membrane, whose hole radius and lattice constant can be tuned to reflect light at a wavelength of choice. When fabricated from materials with low optical absorption such as low-pressure chemically vapor-deposited silicon nitride (LPCVD SiN), one can realize mirrors with subwavelength thicknesses and reflectivities > 99 %, only limited by scattering losses [8]. LPCVD SiN thin films also enable the combination of PhC mirrors with low thermal noise mechanical oscillators, due to their high intrinsic stress, thin geometry, and weak coupling to undesired thermal modes [6, 13].

Limitations in microfabrication processes have so far restricted suspended PhC mirrors to areas not much bigger than $100 \times 100\,\mu\mathrm{m}^2$. This size sets an upper bound to the waist of incident Gaussian beams, since wider waists do not completely interact with the PhC, resulting in decreased reflectivity. But the beams also have a lower bound, since very small waists have a high divergence and couple to undesired PhC modes, which leads to shifting, broadening and shallowing of the reflectivity. These adverse finite-size effects have been consistently measured in very thin mirrors with thicknesses below 0.1λ, where λ is the wavelength of the reflected light [6, 7, 14, 15]. The ability to fabricate larger PhC mirrors with increasingly thinner membranes could greatly facilitate the combination of high reflectivity and low mechanical clamping losses [6]. These properties are crucial for reducing thermal mirror coating noise which stands as a limit in precision measurements such as atomic clocks [16], frequency-stabilized lasers [17], and gravitational wave detectors [18]. At the centimeter scale, PhC mirrors could have more immediate applications as deformable mirrors with adjustable wavefront [4], or evanescent field sensors with a large interaction area [2, 3].

Scaling up suspended PhC mirrors even further to meter scales would make this technology compatible with a number of next-generation experiments. Some of the most promising avenues for interstellar exploration, for example, rely on the development of low-mass light sails (i.e. lightweight reflectors), which could be accelerated to 1/5 the speed of light using radiation pressure [1]. Initiatives like the Starshot Breakthrough [19] require meter-sized light sails with a thickness of only tens of nanometers – an aspect-ratio that is far beyond current nanotechnology and that stands out as one of the most daunting challenges of this ambitious project.

In this letter we experimentally demonstrate free-standing SiN photonic crystal mirrors with thicknesses of 56 and 210 nm and diameters of up to 10 mm. Not only do we increase the area of suspended PhC mirrors by nearly 4 orders of magnitude compared to previous works, we also show that these large aspect-ratios allow us to achieve high reflectivity from membranes 3 times thinner than previously measured. We observe greater than 90 % reflectivity of 1550 nm light from mirrors with a thickness of 0.038λ (56 nm) – an experimental first as PhC mirrors have consistently been limited to thicknesses above 0.13λ (210 nm at 1550 nm) to attain high reflectivity [6]. Such large structures allow studying the spec-

* These authors contributed equally to this work.
† r.a.norte@tudelft.nl
‡ s.groeblacher@tudelft.nl

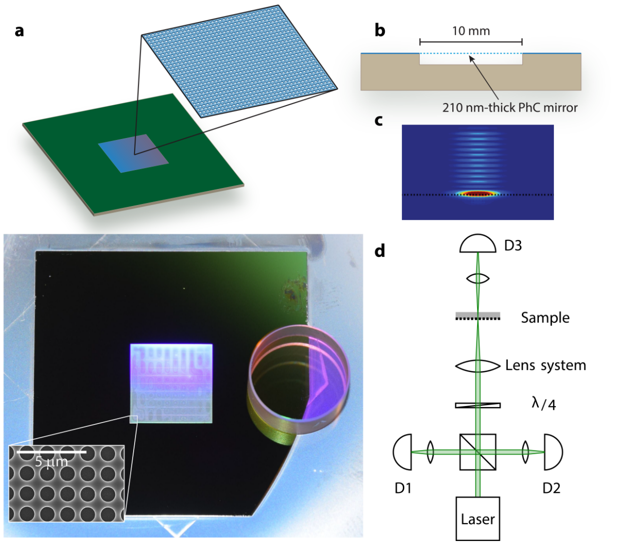

Figure 1. **PhC mirrors and characterization setup. a** Sketch of a suspended PhC mirror (top) and a photograph of a 10 mm-wide, 210 nm-thick PhC mirror next to a commercial 1/2 inch mirror for size comparison (bottom). The rectangular shaped patterns within the PhC are stitching errors from the mainfields of the beamwrite, which do not affect the measured reflectivity significantly. The inset shows a scanning electron microscope picture of the actual photonic crystal. The full mirror is made up of around $6 \cdot 10^7$ holes. **b** Illustration of the cross section of the mirror. The thin membrane is made of SiN and is supported by a silicon chip. **c** FDTD simulation of a reflected light mode on a PhC membrane. **d** Simplified setup used to characterize the reflection of PhC mirrors. We focus a wavelength-tunable laser beam perpendicularly onto the membrane. The radius of the incident beam is controlled with a lens system. For each radius, we acquire the reflection (D2) and transmission (D3) in relation to a reference beam (D1) that is split off the laser output using a polarization beam splitter. More details can be found in the Supplementary Information.

trum of PhC membranes as a function of incident beam waist with less constraints from finite size effects. Additionally we find that their performance becomes insensitive to small defects in the PhC lattice for large beam waists, exemplified through the constant reflectivity despite the presence of fabrication errors in the lithography process for the largest device (see Fig. 1a). This is a key observation for the prospects of extending their nanoengineered features to the meter scale. We also consider how a suspended PhC mirror coating would perform in future gravitational wave experiments at cryogenic temperatures where they could potentially reduce the thermal coating noise. These results push the boundaries of current nanotechnology and represent a significant leap towards bringing the unique properties of optical nanostructures to a completely new scale of experiments.

Our suspended PhC mirrors are fabricated from high-stress (1 GPa) LPCVD SiN films deposited on 200 µm Si wafers. The geometry of the PhC structures is optimized for each desired film thickness to a wavelength of 1550 nm using finite-difference time-domain (FDTD) simulations [5]. The structures are patterned on the SiN films using electron beam lithography and a plasma etching process ($CHF_3 + O_2$). Stitching errors occur about every millimeter due to stage drifts during the beamwrite and are on the order of a 1 µm wide. A hot piranha solution consisting of sulfuric acid and hydrogen peroxide is used to clean the surface of organic contaminations. This is followed by a diluted HF solution to smoothen the SiN surface [20] and remove surface-oxide from the silicon which allows for an even release of the membrane. Finally, we suspend the PhC mirrors using turbulence-free fabrication techniques [21]. Figs. 1a-c show a sketch and a photograph of a 10 mm-wide, 210 nm-thin mirror, in addition to a scanning electron microscope picture of the PhC pattern and numerical simulations of the reflected optical field.

In order to characterize the optical properties of the PhCs, we fabricate three devices with different thickness and size: two 210 nm-thick mirrors, 4 mm and 10 mm-wide; and a 56 nm-thick, 1.6 mm-wide one. The devices are characterized by focusing a wavelength-tunable laser beam perpendicular to the PhC mirrors (Fig. 1d). We measure the reflected and transmitted power and compare it to a reference beam that does not interact with the devices. For calibration, we use a commercial broadband mirror at the same position as the PhC mirrors. The laser is tuned from 1530 to 1630 nm. The recorded signal is normalized to the reference arm and to the calibration mirror to obtain the reflectivity spectra for multiple beam waists. We vary the beam radius between 8 µm and 1.1 mm using a lens system placed in front of the PhC membranes. This allows us to analyze the behavior of PhC membranes with different thicknesses to laser beams of varying sizes.

Fig. 2 shows a selection of measured spectra of the 210 nm-thick, 4 mm-wide and the 56 nm-thick devices. While the PhC is completely released, for testing purposes the chip itself is not fully etched through (cf. Fig. 1b). This results in a parasitic interference pattern with a periodicity of 1.8 nm on top of the expected PhC spectra, corresponding to a 200 µm-thick Si etalon. Since the frequency of this interference is well defined, we post-process it by band-pass filtering the data. The Supplementary Information contains the full set of acquired spectra, as well as a detailed description of the data processing.

The spectra of the 210 nm-thick PhC mirror, shown in Fig. 2a, exhibit a resonance at 1549 nm that varies little with the incident beam waist. At 1573 nm a parasitic resonance emerges whose width increases as the waist becomes smaller. This can be understood by considering the decomposition of a Gaussian beam with waist w_0 into plane waves [22]. The decomposition in terms of incidence angle is weighted by a Gaussian distribu-

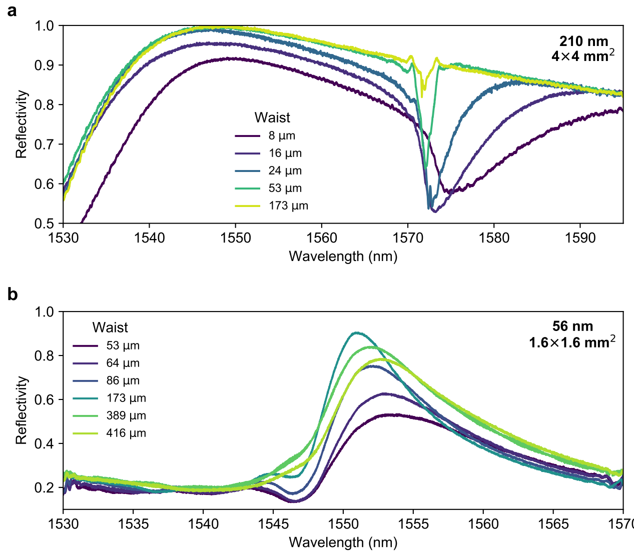

Figure 2. **Reflectivity spectra of the PhC mirrors.** Shown is a selection of measured reflectivity spectra of PhC mirrors with film thickness of **a** 210 nm and **b** 56 nm. Each spectrum shows the reflection of a Gaussian beam with the specified waist. As the waist increases, the incident beam approaches the behavior of a plane wave, for which the devices are optimal, and so the maximum reflectivity increases. Due to the finite size of the 56 nm PhC mirror, its reflectivity drops as the incident beam becomes larger than the PhC area. The data were digitally processed to remove parasitic interferences from the substrate (see Supplementary Information for details).

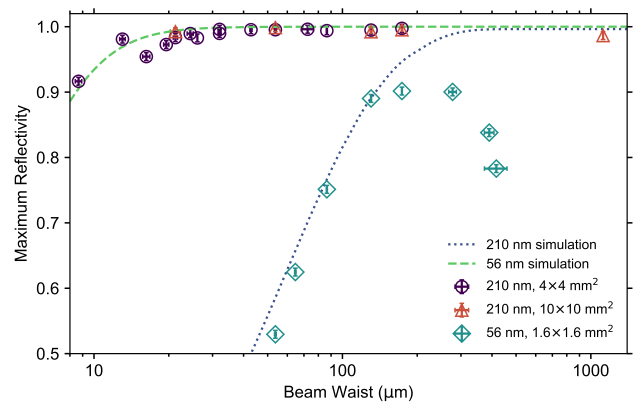

Figure 3. **Maximum reflectivity as a function of incident beam waist.** We show the maximum reflectivity for several PhC thicknesses and membrane sizes, clearly highlighting the potential of these structures as large-area, high-reflectivity mirrors. For comparison, we include simulations, represented by lines, obtained from plane wave decomposition of Gaussian beams using RCWA. The reflectivity of the 56 nm-thick PhC mirror decreases when the optical beam becomes comparable to the PhC diameter, underlining the importance of finite size effects. The measured data have an uncertainty in reflectivity of $\pm 0.6\,\%$. The uncertainty in the beam radii results from propagating the estimated uncertainties in the positions of the lens sets. For more details see the Supplementary Information.

tion with a standard deviation equal to the beam divergence $\theta = \lambda/\pi w_0$. A large waist w_0 has a small divergence θ, which is a good approximation to a plane wave with a zero angle of incidence. As w_0 decreases, θ becomes larger, and so plane waves with larger angles of incidence have a stronger weight on the decomposition. These waves can couple to PhC modes other than the resonance of interest, giving rise to parasitic features such as the one observed. We can apply the same reasoning to explain the increase in maximum reflectivity of the main resonance: the device geometry was optimized assuming a plane wave with normal incidence. Hence, beams with a large waist approximate this condition better, which results in a reflectivity closer to the optimized one.

In Fig. 2b we observe that the main resonance of the 56 nm-thick membrane exhibits stronger shifts in wavelength, width and maximum reflectivity with varying beam waist, in comparison to the 210 nm-thick device. As explained in the work of Bernard et al. [7], the spectral response of plane waves incident on a PhC mirror depends on the angle of incidence. This dependence is stronger for thinner devices and results in large resonance wavelength shifts. Therefore, as the beam waist decreases – and its divergence increases – the reflectivity of thin devices is more strongly attenuated. On the other hand, due to the small size of the 56 nm-thick PhC mirror (diameter of 1.6 mm vs. 4 mm for the 210 nm-thick device) beams with waists larger than 280 µm are partially scattered outside the PhC and exhibit a decreasing maximum reflectivity (see below).

Fig. 3 shows the maximum reflectivity of all PhC membranes as a function of the incident beam waist. As described in the previous paragraphs, larger beam waists approximate the design conditions of the PhCs better, reducing the amount of light that couples to unwanted modes. As such, the maximum reflectivity increases for larger beams. We verify this behavior with simulations and plane wave decomposition: starting with the geometry parameters that resulted from the FDTD optimization and that were patterned on the SiN membranes, we simulate the reflectivity of plane waves with varying angles of incidence at the resonance wavelength using rigorous coupled-wave analysis (RCWA) [23]. The reflectivity at each beam waist is then the weighted sum of the simulation results, following a Gaussian distribution with standard deviation θ, which is further described in the Supplementary Information.

The reflectivity of the 56 nm-thick PhC mirror decreases when the beam radius measures between 280 and 390 µm. Considering that the field amplitude of a Gaussian beam falls as e^{-r^2/w_0^2}, where r is the distance from the beam's center, we expect 99 % of the field to be within

a diameter of $6 \cdot w_0$. Since the PhC is 1.6 mm wide, beams with waists larger than $1.6/6\,\mathrm{mm} = 270\,\mu\mathrm{m}$ will have larger field components reflecting off the area outside the PhC. This allows us to observe a smooth transition between two regimes: one, for small waists, where the PhC response is limited by a large beam divergence and another one for large waists, where the limitation is the finite size of the device. Between these two bounds we see a plateau where the maximum reflectivity >90 % is approximately constant. To the best of our knowledge, this is the highest reported reflectivity of a 56 nm suspended PhC mirror, operating in a regime with lower beam divergence and finite size limits.

In conclusion, we fabricate and characterize the first suspended PhC mirrors that span areas up to square-centimeters, with reflectivities exceeding 99 %, which are only limited by our measurement precision. These measurements could be further improved by using an optical cavity [8]. Previous attempts focused on square-micrometer-large devices, resulting in strong limits to the maximum achievable reflectivity, in particular for devices thinner than 0.13λ. By measuring the reflectivity spectrum of the PhC mirrors for varying incident beam waists, our work shows that these devices are indeed strongly affected by finite size effects. In particular, we observe a reflectivity of 90 % for a 0.03λ-thick PhC mirror at a wavelength of 1550 nm, whereas previous reports of devices with similar thickness were limited to about 56 % [7, 15]. It is also important to note that these mirrors could be improved even further with more sophisticated methods of lithography. Electron beam lithography is prone to stage drifts during exposure and secondary back-scattering of electrons from the substrate which produce uneven dosing – both of these effects can lead to an inhomogeneous lattice constant and variations in hole size. Since larger incident beams sample a larger area of the PhC structure, we observe that the reflectivity is indeed robust to imperfections in the 2D array of holes that arise from drifts or poor stitching during lithography. We envision scaling these devices further by using techniques such as nano-imprint lithography, lithography stepping, or interference lithography [24].

Proposals using large light sails like the Starshot Breakthrough, require mirrors with lateral sizes of $4 \times 4\,\mathrm{m}^2$, thicknesses of 0.05λ, reflectivities of 90 %, ppm-level optical absorption and a total mass of only 1 g [19]. Our PhC are designed with a lattice of holes which remove about 30 % of the mass of the membrane. Additionally, they are made of LPCVD SiN which has an imaginary refractive index of about 10^{-6} at 1064 nm and has been shown to withstand high laser powers of around $2.5 \cdot 10^{11}\,\mathrm{W/m}^2$ [21] – nearly 2 orders of magnitude more than what is required for the initiative. Our mirrors mark the first proof-of-concept which could realistically be implemented at larger scales for the Starshot Breakthrough Initiative. The high intrinsic tensile stress of LPCVD SiN allows to expand these mirrors to large diameters while remaining relatively flat. This is a crucial feature for the fabrication of continuous, suspended films with enough stability to avoid segmented mirror geometries supported by small frames, dramatically decreasing the overall weight of a light sail.

High-stress SiN membranes have also been shown to have high thermal noise suppression which becomes significantly better with thinner, larger membranes [6]. Moreover, the mechanical quality of SiN membrane resonators typically increases by an order of magnitude when cooled to 10 K [25], and by two orders at 10 mK [26]. This is particularly interesting for experiments limited by the thermal displacement noise of conventional mirrors made with SiO_2/Ta_2O_5 distributed Bragg reflector (DBR) coatings [27]. The thermal noise is in general reduced at low temperatures, and experiments like the Einstein Telescope or KAGRA are moving towards cryogenic operation [28, 29]. However, contrary to SiN, the thermal noise of SiO_2/Ta_2O_5 films remains almost unchanged when cooled from 300 K to 10 K [30]. By performing a simple calculation of the thermal displacement noise for suspended PhC mirrors at low temperatures, we estimate that these devices can perform better than standard DBR mirrors (see Supplementary Information). For example, considering the conditions of KAGRA [29], we obtain a thermal displacement noise of $\sqrt{S_x} \approx 3 \cdot 10^{-20}\,\mathrm{m}/\sqrt{\mathrm{Hz}}$, a factor of 2 lower than the performance of KAGRA's DBR mirrors and mainly limited by the base vacuum pressure of the experiment.

Furthermore, the fact that these mirrors are suspended allows them to be used in a variety of applications that profit from mechanical tuning of mirrors. Deformable mirrors could be realized with these PhC structures [4], for example through electrostatic-tuning with arrays of electrodes close to the mirror, or even as displacement noise tunable mirrors, using techniques such as optomechanical feedback control [31]. Further experiments are planned to study the transversal mode composition of the reflected beam. These developments open up a new paradigm in nanotechnology – one that steers away from the focus on simply miniaturizing components, but instead tries to bring the performance of nano-engineered materials to large scales.

We thank F. Alpeggiani, P. Klupar, A. Loeb, and P. Worden for helpful discussions. We also acknowledge valuable support from the Kavli Nanolab Delft, in particular from C. de Boer and M. Zuiddam. This project was supported by the European Research Council (ERC StG Strong-Q) and by the Netherlands Organisation for Scientific Research (NWO/OCW), as part of the Frontiers of Nanoscience program.

[1] P. Lubin, J. Br. Interplanet. Soc. **69**, 40 (2016).
[2] J. H. Schmid, W. Sinclair, J. García, S. Janz, J. Lapointe, D. Poitras, Y. Li, T. Mischki, G. Lopinski, P. Cheben, A. Delâge, A. Densmore, P. Waldron, and D.-X. Xu, Opt. Express **17**, 18371 (2009).
[3] X. Fan, ed., *Advanced Photonic Structures for Biological and Chemical Detection*, 1st ed. (Springer-Verlag, 2009).
[4] P.-Y. Madec, in *Adaptive Optics Systems III*, Vol. 8447 (SPIE, 2012) pp. 844705–1–18.
[5] S. Fan and J. D. Joannopoulos, Phys. Rev. B **65**, 235112 (2002).
[6] R. A. Norte, J. P. Moura, and S. Gröblacher, Phys. Rev. Lett. **116**, 147202 (2016).
[7] S. Bernard, C. Reinhardt, V. Dumont, Y.-A. Peter, and J. C. Sankey, Opt. Lett. **41**, 5624 (2016).
[8] X. Chen, C. Chardin, K. Makles, C. Caër, S. Chua, R. Braive, I. Robert-Philip, T. Briant, P.-F. Cohadon, A. Heidmann, T. Jacqmin, and S. Deléglise, Light Sci. Appl. **6**, e16190 (2017).
[9] M. Kanskar, P. Paddon, V. Pacradouni, R. Morin, A. Busch, J. F. Young, S. R. Johnson, J. MacKenzie, and T. Tiedje, Appl. Phys. Lett. **70**, 1438 (1997).
[10] F. Lu, F. G. Sedgwick, V. Karagodsky, C. Chase, and C. J. Chang-Hasnain, Opt. Express **18**, 12606 (2010).
[11] D. Fattal, J. Li, Z. Peng, M. Fiorentino, and R. G. Beausoleil, Nat. Photon. **4**, 466 (2010).
[12] J. Guo, R. A. Norte, and S. Gröblacher, Opt. Express **25**, 9196 (2017).
[13] C. Reinhardt, T. Müller, A. Bourassa, and J. C. Sankey, Phys. Rev. X **6**, 021001 (2016).
[14] U. Kemiktarak, M. Durand, M. Metcalfe, and J. Lawall, New J. Phys. **14**, 125010 (2012).
[15] C. H. Bui, J. Zheng, S. W. Hoch, L. Y. T. Lee, J. G. E. Harris, and C. W. Wong, Appl. Phys. Lett. **100**, 021110 (2012).
[16] S. L. Campbell, R. B. Hutson, G. E. Marti, A. Goban, N. Darkwah Oppong, R. L. McNally, L. Sonderhouse, J. M. Robinson, W. Zhang, B. J. Bloom, and J. Ye, arXiv:1702.01210 (2017).
[17] T. Kessler, C. Hagemann, C. Grebing, T. Legero, U. Sterr, F. Riehle, M. J. Martin, L. Chen, and J. Ye, Nat. Photon. **6**, 687 (2012).
[18] S. Reid and I. W. Martin, Coatings **6**, 61 (2016).
[19] "Breakthrough Initiative – Starshot," `https://breakthroughinitiatives.org/Initiative/3`, accessed July 2017.
[20] X. Ji, F. A. S. Barbosa, S. P. Roberts, A. Dutt, J. Cardenas, Y. Okawachi, A. Bryant, A. L. Gaeta, and M. Lipson, Optica **4**, 619 (2017).
[21] R. A. Norte, *Nanofabrication for On-Chip Optical Levitation, Atom-Trapping, and Superconducting Quantum Circuits*, Ph.D. thesis, California Institute of Technology (2014).
[22] M. Born and E. Wolf, *Principles of Optics*, 6th ed. (Pergamon Press, 1986).
[23] M. G. Moharam and T. K. Gaylord, J. Opt. Soc. Am. **71**, 811 (1981).
[24] C. Lu and R. H. Lipson, Laser Photon. Rev. **4**, 568 (2010).
[25] B. M. Zwickl, W. E. Shanks, A. M. Jayich, C. Yang, A. C. Bleszynski Jayich, J. D. Thompson, and J. G. E. Harris, Appl. Phys. Lett. **92**, 103125 (2008).
[26] M. Yuan, M. A. Cohen, and G. A. Steele, Appl. Phys. Lett. **107**, 263501 (2015).
[27] The LIGO Scientific Collaboration, Class. Quantum Grav. **32**, 074001 (2015).
[28] The ET science team, "Einstein gravitational wave telescope – conceptual design study," `https://tds.virgo-gw.eu/ql/?c=7954` (2011).
[29] Y. Aso, Y. Michimura, K. Somiya, M. Ando, O. Miyakawa, T. Sekiguchi, D. Tatsumi, and H. Yamamoto (The KAGRA Collaboration), Phys. Rev. D **88**, 043007 (2013).
[30] I. W. Martin, R. Bassiri, R. Nawrodt, M. M. Fejer, A. Gretarsson, E. Gustafson, G. Harry, J. Hough, I. MacLaren, S. Penn, S. Reid, R. Route, S. Rowan, C. Schwarz, P. Seidel, J. Scott, and A. L. Woodcraft, Class. Quantum Grav. **27**, 225020 (2010).
[31] H. M. Wiseman, Phys. Rev. A **49**, 2133 (1994).
[32] D. R. Rhodes, Proc. IEEE **52**, 1013 (1964).
[33] V. Liu and S. Fan, Comput. Phys. Commun. **183**, 2233 (2012).
[34] Y. Tsaturyan, A. Barg, E. S. Polzik, and A. Schliesser, Nat. Nanotechnol. (2017).
[35] P. R. Saulson, Phys. Rev. D **42**, 2437 (1990).
[36] D. J. Wilson, *Cavity Optomechanics With High-Stress Silicon Nitride Films*, Ph.D. thesis, California Institute of Technology (2012).
[37] S. Schmid, K. D. Jensen, K. H. Nielsen, and A. Boisen, Phys. Rev. B **84**, 165307 (2011).
[38] S. Chakram, Y. S. Patil, L. Chang, and M. Vengalattore, Phys. Rev. Lett. **112**, 127201 (2014).
[39] M. Bao, H. Yang, H. Yin, and Y. Sun, J. Micromech. Microeng. **12**, 341 (2002).
[40] K. Somiya, Class. Quantum Grav. **29**, 124007 (2012).
[41] D. J. Wilson, *Cavity optomechanics with high-stress silicon nitride films*, Ph.D. thesis, California Institute of Technology (2012).
[42] G. D. Cole, W. Zhang, M. J. Martin, J. Ye, and M. Aspelmeyer, Nat. Photon. **7**, 644 (2013).

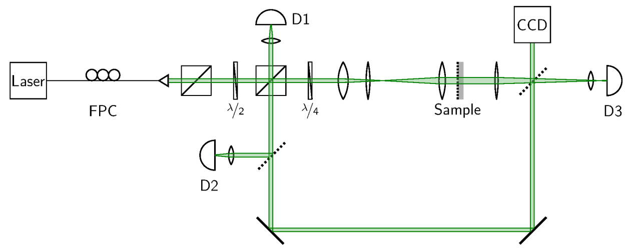

Figure S1. **Schematic of the complete characterization setup.** See text for a detailed description.

SUPPLEMENTARY INFORMATION

Setup

In order to characterize the optical properties of the PhCs, we use the setup outlined in Fig. S1. A fiber coupled Santec TSL510 wavelength-tunable laser is used as a light source. Its polarization is adjusted with a fiber polarization controller (FPC) and the beam is brought into free-space using a triplet collimator (Thorlabs TC12APC-1550). The first polarization beam splitter (PBS) is used as a polarizer to mitigate the effect of polarization drifts in the fiber part of the setup. The second PBS splits light into the beam that is going to interact with the sample (incident beam), and a reference beam that is detected by D1. We use the reference beam to remove the effect of power oscillations from the measured spectra that are not related to the sample. Between the two PBSs we place a half-waveplate ($\lambda/2$) to control the power ratio between the incident and reference beams. After the second PBS, the incident beam is focused onto the sample using a lens set (between 1 and 3 lenses) which are adjusted to change the waist from 8 to 420 µm. Light reflected by the sample is sent into the second PBS. We place a quarter-waveplate ($\lambda/4$) in the incident beam path such that the reflected beam is separated from the incident beam by the PBS and then detected by D2. Light transmitted by the sample is recorded by D3.

For every lens system a commercial broadband-coated mirror is placed at the sample position and record reference and reflection spectra. These serve as calibration and remove effects such as losses in the optical path from the sample reflectivity spectra. The sample is then placed back and care is taken to ensure good tip/tilt alignment with respect to the optical beam, since the response of the PhC is very sensitive to the incident angle. Using flip mirrors we are also able to send the transmitted or reflected beam into an infra-red CCD. The camera helps during the tip/tilt alignment of the sample, or acts as a reference during the alignment of the lens system.

The reflectivity spectrum R is calculated as

$$R = \frac{V_{\mathrm{PhC}}/V_{\mathrm{PhC}}^{\mathrm{ref}}}{V_{\mathrm{cal}}/V_{\mathrm{cal}}^{\mathrm{ref}}} \cdot R_{\mathrm{cal}},$$

where V_{PhC} and V_{cal} are the voltage signals of the reflected beams from the PhC and the calibration mirror, $V_{\mathrm{PhC}}^{\mathrm{ref}}$ and $V_{\mathrm{cal}}^{\mathrm{ref}}$ are the reference signals of the corresponding PhC and calibration mirror measurements, and R_{cal} is the reflectivity of the calibration mirror, which is specified to be 99.8(3) %. We consider all measurement uncertainties to be independent from each other, and estimate the uncertainty in reflectivity ΔR via the method of uncertainty propagation

$$\Delta R = \sqrt{\sum_x \left(\frac{\partial R(x)}{\partial x} \Delta x \right)^2} \approx 0.006,$$

where $x = \{V_{\mathrm{PhC}}, V_{\mathrm{PhC}}^{\mathrm{ref}}, V_{\mathrm{cal}}, V_{\mathrm{cal}}^{\mathrm{ref}}, R_{\mathrm{cal}}\}$.

To estimate the uncertainty of the beam waist, the same propagation method was applied. As uncertainty parameters, the position of each lens (with a count varying between 1 and 3) and its focal length is taken into account. The beam was propagated through the lens system by means of the complex beam parameter and ABCD matrices.

The photodetectors D1, D2, D3 are home-built surface-mount-device circuits equipped with a JDSU ETX500 photodiode. By means of electronic design and spectral characterization, a linear response to the optical input power is guaranteed.

Post-Processing of Spectral Data

Fig. S2 shows the full, unprocessed set of measured reflectivity spectra for the (a) 210 nm and (b) 56 nm-thick devices. We measured the spectra for several incident beam waists, which are indicated in the figure legends. The spectra follow the expected Fano resonance shape, characteristic for this type of device.

In addition, we also see a parasitic oscillation with a periodicity of 1.8 nm. This is because the devices are suspended but the substrate is not etched through. In fact, to facilitate the testing process, the membranes are undercut by only a few µm on top of the 200 µm silicon substrate. The observed periodic pattern arises from interference of reflections from the substrate interfaces. Using the thickness of the silicon substrate and a refractive index of 3.5, we calculate a free spectral range of 1.7 nm for a wavelength of 1550 nm, which is in excellent agreement with the observed oscillations. The periodicity observed on the measured spectra is equal for all measurements and as such, we remove it digitally using the procedure described below.

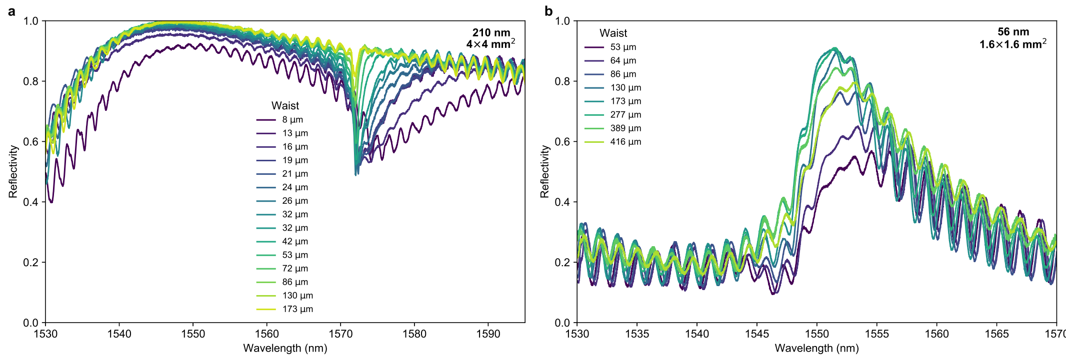

Figure S2. **Unprocessed reflectivity spectra of the PhC mirrors.**

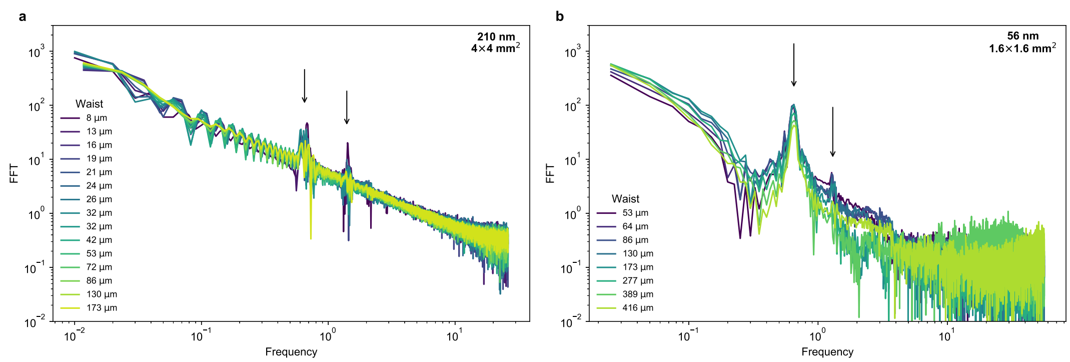

Figure S3. **Fourier transformations of the unprocessed optical spectra.**

The Fourier transformations of the unprocessed reflectivity spectra show peaks (marked by the arrows in Fig. S3) that are well defined and common to all measurements, which we associate with the described etalon effect. These are obtained with the `fft.rfft` and `fft.rfftfreq` commands of the Python `numpy` library. To remove these parasitic features from the Fourier transforms, we apply a Tukey filter, with filter parameter 0.9, around the identified peaks. The filter was generated using the function `signal.tukey` from the `scipy` library. Finally, the filtered spectra are obtained by performing the inverse Fourier transform using the `fft.irfft` command. These can be seen in Fig. S4. We carefully verify that filtering does not change the reading of the maximum reflectivity.

Fig. S5 shows the raw data of the 210 nm-thick, 10 mm-wide device. This device was attached to a single-side polished carrier wafer using an index matching oil. Since the bottom surface of the substrate is rough, the interference between interfaces is no longer visible. Therefore this data set did not require any post-processing.

Simulated reflectivity spectra for Gaussian beams

To simulate the expected reflectivity spectra of the PhC membranes, we use a rigorous coupled wave analysis (RCWA) [23] combined with a plane wave decomposition [32]. On the one hand, choosing a RCWA implies that the simulated spectra are valid only for periodic structures, i.e. spectral changes caused by diffraction effects at the membrane's edge cannot be recreated. As this approach commonly starts with a plane wave as the incident electromagnetic field, it also requires to implement a composition of plane wave spectra when dealing with Gaussian beams. On the other hand, a finite element analysis (FEA) can in principle be set up to compute spectra of a finite, e.g. $10 \times 10\,\mathrm{mm}^2$ large, PhC membrane excited by a Gaussian beam of waist w_0. However, the simplicity of a FEA approach has disadvantages when it comes to hardware, especially memory, requirements. To faithfully simulate the structure, the model volume has to cover about $20 \times 20 \times 1\,\mathrm{mm}^3$ and still capture the details of the nano-scale membrane, which increases the memory usage drastically. A RCWA only discretizes the actual PhC membrane, such that the reflected field can be retrieved at any point above or below the structure. Finally, having simulated a set of plane waves via RCWA allows to assemble Gaussian

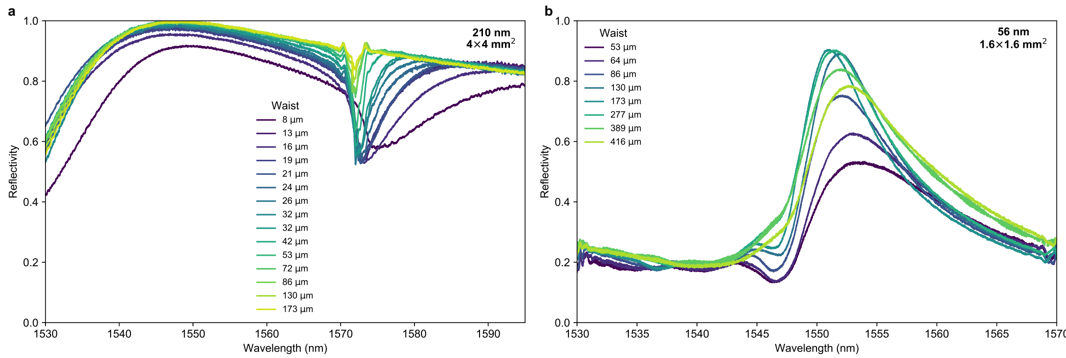

Figure S4. **Filtered reflectivity spectra of the PhC mirrors.**

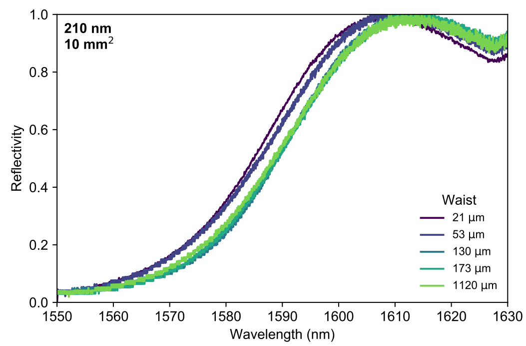

Figure S5. **Unprocessed reflectivity spectra of the 210 nm-thick, 10 mm-wide device.**

beams of any size. For our requirements, the RCWA approach therefore is most appropriate.

We simulate two different unit cells:

- 210 nm thick, lattice constant 1.355 µm, hole radius 0.5014 µm
- 56 nm thick, lattice constant 1.526 µm, hole radius 0.6265 µm.

Each cell, composed of 140 modes, is excited at a certain wavelength with 66^2 plane waves of various polar and azimuthal angles of incidence. To verify that the structure is polarization insensitive, the wavelength- and angle scan is conducted for both s- and p-polarization. The simulation is built around an open source RCWA package [33], which rotates the s and p component of the incident field with respect to the incident angles. To align the polarization uniformly for all angles, the s- and p-electric field component E are transformed as

$$E_s \mapsto \cos(\theta)/\cos(\phi) \tag{S1a}$$

$$E_p \mapsto -\sin(\theta) \tag{S1b}$$

and

$$E_s \mapsto \sin(\theta)/\cos(\phi) \tag{S2a}$$

$$E_p \mapsto \cos(\theta) \tag{S2b}$$

for a s- and p-polarized beam, respectively. Here the polar angle is denoted by ϕ, while θ is the azimuthal angle. This set of transformations inverts the global rotation implemented in the software package.

Having computed the reflection coefficients $r_{s,p}(\phi, \theta, \lambda) \in \mathbb{C}$ for a plane wave, the reflectivity of a Gaussian beam with the electric field distribution

$$E(x, y) = \sqrt{\frac{2}{\pi w_0^2}} e^{-\frac{x^2+y^2}{w_0^2}} \tag{S3}$$

at the waist position ($z = 0$) is obtained by weighting the reflection coefficients according to the plane wave decomposition

$$E(k_x, k_y) = \iint_{-\infty}^{\infty} E(x, y) e^{\imath(k_x x + k_y y - \frac{2\pi c_0}{\lambda} t + \phi)} \mathrm{d}x\mathrm{d}y. \tag{S4}$$

Transforming the expression to spherical coordinates, the power reflectivity spectra are computed via

$$R_{s,p}(\lambda, w_0) = \frac{\iint |r_{s,p}(\phi, \theta, \lambda)|^2 e^{-\frac{1}{2}(w_0 r \sin(\phi))^2} \sin(\phi)\mathrm{d}\theta\mathrm{d}\phi}{\iint e^{-\frac{1}{2}(w_0 r \sin(\phi))^2} \sin(\phi)\mathrm{d}\theta\mathrm{d}\phi}. \tag{S5}$$

Fig. S6 illustrates the results of the simulations for a 56 nm and 210 nm unit cell with the parameters given

above. Due to a small mismatch in the cell parameters the absolute resonance frequency of the measured and simulated spectra deviate from each other slightly, however the overall features of the measurement are recreated faithfully. The individual simulations of s- and p-polarization exhibit virtually no difference, which is an important as we probe the membranes with a circularly polarized beam. From the data plotted in Fig. S6, the maximum achievable reflectivity can be readily extracted by determining the peak reflectivity for each wavelength and beam waist scan. In figure S7 the results from the main text are plotted again and the simulated maximum reflectivity is shown for both polarizations. A zoom into the last two percent helps reading out the measured values.

Estimation of Thermal Displacement Noise

Thermal mirror coating noise is currently one of the main limitations to the sensitivity of high-precision experiments including atomic clocks, frequency stabilized lasers and gravitational wave detectors. Future iterations of these applications aim to operate mirrors at cryogenic temperature where they can reduce the overall thermal noise and increase their sensitivities [28, 29]. Widely-used distributed Bragg mirror coatings made from SiO_2 and TiO_2-doped Ta_2O_5 have a slightly better noise performance at low temperatures, but this is still within an order of magnitude of the noise at room temperature [30]. In contrast, LPCVD SiN high-stress membranes have shown enhanced mechanical quality factors by over 2 orders of magnitude at cryogenic temperatures [6, 13, 26, 34] compared to its state-of-the-art performance at room temperature. In addition, whereas DBR coatings usually consist of nearly 30-40 layers to attain high reflectivity (each with a thickness of 0.25λ), PhC mirrors can realize high reflectivity with a thin membrane which is only a fraction of the thickness of a single DBR layer.

In this section we perform a simplified calculation of the thermal noise performance of suspended PhC mirrors and compare it to the thermal coating noise of the aLIGO, Einstein Telescope (ET) or KAGRA gravitational wave detectors. For large LPCVD SiN mirrors we estimate the biggest noise contribution to be due to the thermal displacement noise, which for a square membrane is given by [35]

$$S_x(\omega) = \frac{4k_B T m_{\mathrm{eff}} \omega_{\mathrm{m}}/Q}{m_{\mathrm{eff}}^2((\omega^2-\omega_{\mathrm{m}}^2)^2 + (\omega_{\mathrm{m}}\omega/Q)^2)}, \tag{S6}$$

where Q is the mechanical quality factor, k_B the Boltzmann constant, T is the membrane's temperature, m_{eff} the effective mass of the membrane's fundamental mode, and ω_{m} its frequency.

	aLIGO	ET	KAGRA
L (mm)	350	500	250
p (hPa)	$7\cdot10^{-9}$	$1\cdot10^{-10}$	$2\cdot10^{-9}$
$\omega/2\pi$ (Hz)	100	10	100
DBR $\sqrt{S_x}$ (m/$\sqrt{\mathrm{Hz}}$)	$1\cdot10^{-20}$	$1\cdot10^{-21}$	$6\cdot10^{-20}$
m_{eff} (mg)	12	25	6
$\omega_{\mathrm{m}}/2\pi$ (Hz)	1200	860	1700
$T = 10\,\mathrm{mK}$			
Q_{p}	$1\cdot10^{7}$	$6\cdot10^{8}$	$6\cdot10^{7}$
Q_{al}	$3\cdot10^{11}$	$4\cdot10^{11}$	$2\cdot10^{11}$
PhC $\sqrt{S_x}$ (m/$\sqrt{\mathrm{Hz}}$)	$9\cdot10^{-20}$	$2\cdot10^{-20}$	$3\cdot10^{-20}$
$T = 20\,\mathrm{K}$			
Q_{p}	$6\cdot10^{8}$	$3\cdot10^{10}$	$3\cdot10^{9}$
Q_{al}	$3\cdot10^{10}$	$4\cdot10^{10}$	$2\cdot10^{10}$
PhC $\sqrt{S_x}$ (m/$\sqrt{\mathrm{Hz}}$)	$6\cdot10^{-19}$	$1\cdot10^{-19}$	$2\cdot10^{-19}$

Table I. Estimates of thermal displacement noise of suspended PhC mirrors in the context of the aLIGO, ET and KAGRA experiments [27–29, 40].

The mechanical frequency of a square membrane is given by

$$\omega_{\mathrm{m}} = \frac{2\pi}{\sqrt{2}L}\sqrt{\frac{\sigma}{\rho}}, \tag{S7}$$

where L is the length the membrane, ρ is the density of SiN ($2.7\,\mathrm{g/cm^3}$), and σ is the tensile pre-stress in the film, which we take to be 1 GPa. The effective mass can be estimated with $m_{\mathrm{eff}} = m/4$ [36], where m is the physical mass. It is further reduced by a factor of 0.3, which accounts for the mass lost to the PhC holes.

There are numerous limiting factors to the mechanical quality of a membrane [37, 38]: thermoelastic damping, surface defects, Akhiezer damping, etc. For LPCVD SiN membranes, the most relevant factors are acoustic radiation losses and damping from collisions with gas particles. The acoustic radiation losses into the substrate generally scale as the ratio between L and the thickness h: $Q_{\mathrm{rl}} \propto L/h$ [37, 38]. Considering previously measured radiation limited quality factors of $4\cdot10^7$ for $L/h = 5\cdot10^4$, we can extrapolate the radiation limit for arbitrary sizes of the PhC mirror. In addition, the quality factor limited by the gas damping is given by [39]

$$Q_{\mathrm{p}} = \left(\frac{\pi}{2}\right)^{\frac{3}{2}} \rho h \frac{\omega_{\mathrm{m}}}{2\pi}\sqrt{\frac{RT}{m_g}}\frac{1}{p}, \tag{S8}$$

where R is the ideal gas constant, p is the pressure, and m_g is the molecular mass of the background gas molecules. The final Q is given by $Q^{-1} = \sum_i Q_i^{-1}$, where Q_i are the various contributions mentioned above.

Assuming a SiN film thickness of 210 nm and temperatures of 10 mK and 20 K, Tbl. I shows estimates of the thermal displacement noise of PhC mirrors in the conditions of the aLIGO, ET and KAGRA experiments. We

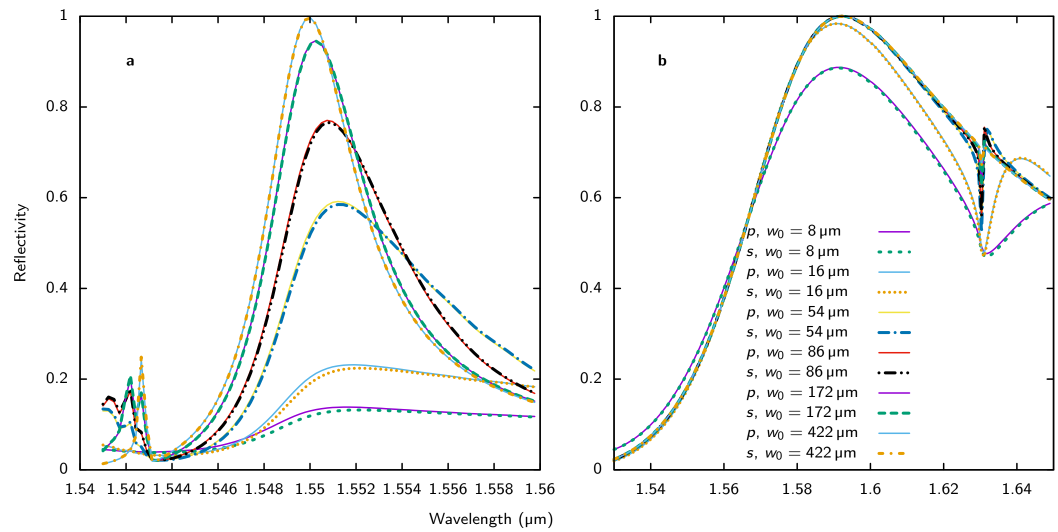

Figure S6. **Reflectivity simulations for PhC membranes.** Reflectivity spectra for s- and p-polarized Gaussian beams of waist w_0. Panel **a** and **b** show data for a 56 nm and 210 nm membrane, respectively.

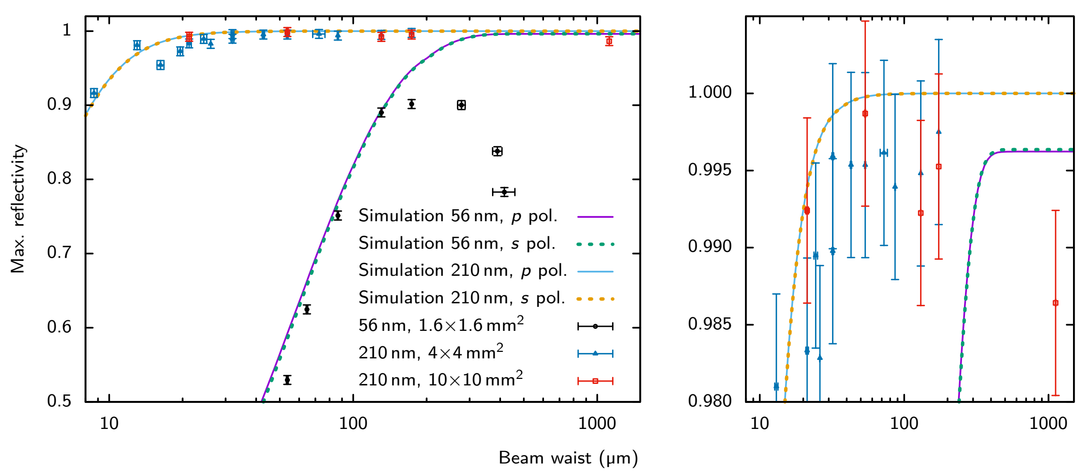

Figure S7. **Extracted peak reflectivity compared to measured data.** Shown is the same data as in the main text with additional simulations for various polarizations.

assume that the main background gas component is hydrogen [27]. From these calculations we notice that the thermal displacement noise of cryogenically cooled PhC mirrors becomes comparable to the thermal coating noise of the DBRs used in the mentioned experiments. These estimates are mainly limited by the environment pressure, which sets an upper bound to the mechanical quality factor. By decreasing the pressure further it should be possible to improve the thermal displacement noise significantly. Furthermore, suspended mirrors have the additional advantage that they can be adjusted, for example either through the addition of tuning electrodes or optomechanical techniques, in order to further reduce the noise performance in the desired regime. Given these parameters, our suspended mirrors do not only have the potential to improve future gravitational wave detectors but also a range of other precision measurements (see main text).

It is important to note that the focus of this calculation is the thermal Brownian noise associated with the mirror coatings. It is however not entirely clear for example, how the Brownian noise related to the substrate would behave for such a suspended mirror. This could be relevant for monolithic cavities in quantum optomechanics experiments at room temperature, where substrate thermal noise is the dominant source of heating in laser cooling experiments [41]. In addition, it has been shown that at increasingly large aspect ratios the substrate thickness becomes a significant variable in a membrane's mechanical quality factor [6]. How these effects translate

to the cm-scale remains an open question. Finally, we would like to point out that crystalline DBRs [42] have been able to perform an order of magnitude better than DBRs made from amorphous layers of SiO_2/Ta_2O_5 at 300 K and can increase their noise performance even further at cryogenic temperature.